

Non-integer harmonics generation by photon acceleration in rapidly evolving nonlinear semiconductor metasurfaces

Maxim R. Shcherbakov,^{1,*} Kevin Werner,² Zhiyuan Fan,¹ Noah Talisa,² Enam Chowdhury,² and Gennady Shvets^{1,†}

¹*School of Applied and Engineering Physics, Cornell University, Ithaca, NY 14853, USA*

²*Department of Physics, The Ohio State University, Columbus, OH 43210, USA*

(Dated: May 13, 2022)

Optical harmonics generation is one of the most fundamental nonlinear frequency conversion effects, whereby an integer number of low-energy photons merge into a single high-energy photon inside a nonlinear material. Here, we report an experimental demonstration of non-integer harmonics generation from mid-infrared light in a resonant silicon metasurface. We show that the acceleration of mid-infrared photons trapped inside the metasurface, triggered by the rapid evolution of the metasurface resonance due to free carrier generation, is responsible for the generation of upconverted photons with peak frequencies of up to $\approx 3.1\omega$. A simple model of resonant photon acceleration is in good agreement with experimental results, and shows a clear path for higher photon acceleration efficiency, which is estimated to be around 22% in our experiments.

Before the demonstration of the first laser by Theodore Maiman, light propagation was widely considered to be a linear process, with the photons not expected to interact with each other. This simple understanding of light-matter interactions was overturned in the early 1960's in second harmonic generation experiments by Franken *et al.* [1]. From this demonstration of the merger between two photons into a photon with doubled energy, the nonlinear optics was born. Subsequent realizations of the third [2] and higher-order [3] harmonics enabled efficient light sources [4], high-resolution microscopy [5, 6], and produced some of the most sensitive optical characterization techniques [7–9].

However, fundamental effects limit the efficiency and spectral range of the canonical nonlinear processes. Mainly, the very nature of the standard n -photon processes (where $n \geq 2$ is an integer) dictates that a narrow-band laser pulse centered at the frequency ω_L with the spectral width $\Delta\omega_L$ cannot produce upconverted photons with the frequencies Ω_n outside of the $|\Omega_n - n\omega_L| \lesssim \sqrt{n}\Delta\omega_L$ spectral interval. While using high-finesse optical cavities or other resonant structures can enhance the efficiency of harmonics generation, they even further limit the spectral range of the nonlinearly generated photons. Thus, a fundamental challenge is to find a nonlinear optical process that enables efficient nonlinear frequency conversion, yet does not sacrifice the spectral width, and is not constrained by the integer frequency condition. In this Article, we utilize one such process: up-conversion of mid-infrared (MIR) light undergoing rapid blue-shifting—also known as photon acceleration [10]—in a resonant nonlinear metasurface.

The concept of photon acceleration (PA) was originally introduced in gaseous plasmas [11, 12] as a process of frequency conversion that occurs when electromagnetic waves propagate in a medium with a time-dependent refractive index [13]. For example, a reduction of the refractive index via free carrier (FC) generation results in a measurable blue-shifting regardless of whether the

FCs were produced by the radiation itself [11, 14] or by an auxiliary electromagnetic pulse [15], as well as in the broadening of the spectrum [16], which was demonstrated for harmonics generation as well [17]. PA in a solid (e.g., semiconductor) medium can be achieved at much lower laser intensities than in a gas because of the ease of FC generation, and can be further enhanced in high quality factor (high- Q) optical cavities. For example, loading photons into a ring microcavity [18] or a photonic crystal cavity [19] and subsequently generating FCs by an external pump while the photons are still in the cavity resulted in continuous near-infrared wavelength shifts of up to 8 nm [20].

Recently, a new paradigm of regularly nanostructured surfaces—metasurfaces [21–23]—has been established for ultra-thin nonlinear and active materials [24, 25]. While metasurfaces share with optical cavities the attractive properties of high spectral selectivity and strong field concentration, their important feature is the strong coupling to free-space beams. A variety of metasurface designs have been implemented for applications as diverse as wave front manipulation [26], rapid amplitude and phase modulation [27–30], as well as the nonlinear applications such as efficient harmonics generation [31–33] and all-optical modulation [34–36]. Of particular interest are semiconductor-based metasurfaces that utilize strong, geometry-dependent Mie-type localized modes [37] with exceptionally high Q -factors [1, 38]. They have already shown record-breaking nonlinear-optical performance [40–43], making them an attractive platform for observing PA and generating non-integer optical harmonics.

Here, we design and experimentally realise an ultra-thin ($h < \lambda/5$; see Fig. 1a for geometry definitions) photon accelerating semiconductor infrared metasurface (PASIM) that undergoes rapid refractive index change due to highly-nonlinear photoinduced generation of free carriers in silicon by a MIR pulse. The PASIM metasurface is designed to have a high- Q resonance at $\lambda_R \equiv$

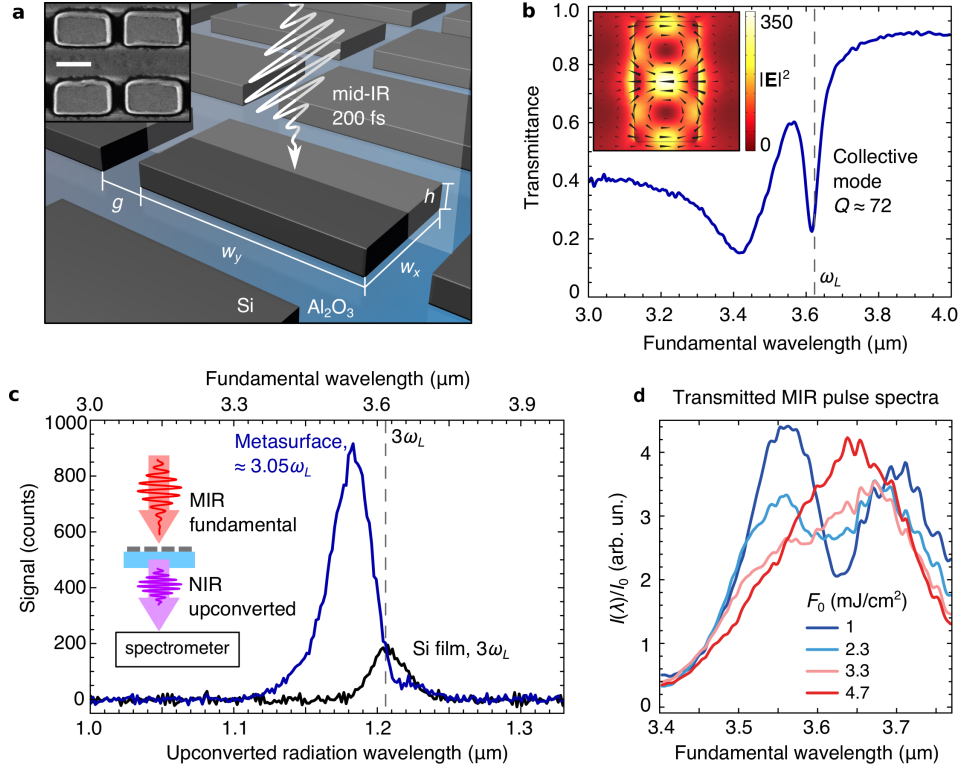


FIG. 1. Nonlinear photon accelerating semiconductor infrared metasurface (PASIM) for non-integer optical harmonics generation. **a**, Schematic of the sample and the MIR beam setup. In experiments, the following dimensions of the sample were used: $w_x = 0.87 \mu\text{m}$, $w_y = 1.54 \mu\text{m}$, $g = 400 \text{ nm}$, and $h = 600 \text{ nm}$. Inset: a close-up scanning electron micrograph of the metasurface elements; scale bar: $1 \mu\text{m}$. **b**, Transmittance spectra of the metasurface measured using FTIR spectroscopy. Dashed line: central wavelength λ_L of the MIR fs pulses. Inset: simulated electric field \mathbf{E} (arrows) and intensity $|\mathbf{E}|^2$ (color) inside a metasurface unit cell for the incident light at $\lambda = \lambda_L$. **c**, Experimentally measured THG in the metasurface (blue curve) and in an unstructured Si film (black curve) of the same thickness h . Both spectra are measured at the same MIR fluence of $F = 2.3 \text{ mJ/cm}^2$ (peak intensity $I = 11 \text{ GW/cm}^2$). A notable blue-shift of the upconversion peak from the metasurface with respect to the expected third harmonic generation is a result of the plasma-induced acceleration of MIR photons. **d**, Spectra of MIR pulses transmitted through the metasurface for different input fluences revealing significant pulse self-modulation.

$2\pi c/\omega_R = 3.62 \mu\text{m}$ that enables efficient four-photon FC generation at modest pulse intensities. This enables us to clearly observe the effect of PA on harmonics generation, with the peaks of the upconverted radiation appearing at frequencies of up to $\approx 3.1\omega_L$, where ω_L is the central frequency of the MIR pulses chosen at $\omega_L \approx \omega_R$ to maximize the effect. An intuitive coupled mode theory model with time-dependent eigenfrequency $\omega_R(t)$ and damping factor $\gamma_R(t) = \omega_R(t)/Q_R(t)$ (where $Q_R(t)$ is a time-dependent quality factor of the metasurface) accurately captures most features of the experimental data and provides further insights into PA efficiency improvements, thus paving the way to future applications utilizing non-stationary nonlinear nanophotonics.

RESULTS

Metasurface design and fabrication. The metasurface was engineered to enhance the local fields, which

is crucial for the efficiency of the nonlinear photon conversion. In our design of the metasurface, we make use of high- Q collective resonances common in regular arrays of semiconductor particles [1, 38, 44]. The specific implementation of the PASIM comprised of nearly-touching domino-shaped Si nanoantennas is shown in Fig. 1a. The quality factor of the resonance—and, hence, the local field enhancement—is controlled by the gap g between the dominos (see the Supplementary Note 1 for ultrahigh $Q \sim 10^4$ designs). For photon acceleration of broadband femtosecond laser pulses, the Q -factor of the PASIM was designed to be moderate: $Q_R \approx 72$, as experimentally confirmed by Fourier-transform infrared (FTIR) spectroscopy measurements using collimated beams [38], as shown in Fig. 1b. Using full-wave simulations, we determine the local MIR field enhancement to be $|\mathbf{E}_{\text{loc}}/\mathbf{E}_0|^2 = 350$, where \mathbf{E}_0 is the amplitude of the incident electric field polarized along the short dimension of the domino. The sharpness of the resonance is attributed to its very small dipole strength due to the near-complete cancel-

lation between positive and negative polarization densities inside the nanoantennas [45] as shown in the inset of Fig. 1b. The samples were fabricated according to a standard procedure described in Methods and Supplementary Note 2.

Upconversion spectroscopy. We focused a $\tau_L \approx 200 \pm 30$ fs MIR laser pulses centered at $\lambda_L = 3.62 \mu\text{m}$, with a variable non-destructive fluence in the $1 < F < 6 \text{ mJ/cm}^2$ range, onto the PASIM to achieve $5 < I < 30 \text{ GW/cm}^2$ intensity (see Supplementary Note 3 for the details of the optical setup). The advantage of operating the PASIM in the MIR regime is that the refractive index change scales as $\Delta n(t) \propto -N_{\text{FC}}(t)\lambda^2$, which will be crucial for PA; here, $N_{\text{FC}}(t)$ is the time-dependent FC density. The third-order nonlinear polarization, which is responsible for the third harmonic generation (THG), can be expressed in the perturbative regime as follows:

$$\mathbf{p}^{(3)}(3\omega) = \hat{\chi}^{(3)}(3\omega = \omega + \omega + \omega) : \mathbf{E}(\omega) \mathbf{E}(\omega) \mathbf{E}(\omega), \quad (1)$$

where $\hat{\chi}^{(3)}(3\omega = \omega + \omega + \omega)$ is the third-order nonlinear susceptibility tensor of silicon, and $\mathbf{E}(\omega)$ is the local electric field strength at the pump frequency ω . Although the resonant local field is confined to a very small volume of each nanoantenna, the cubic dependence of $\mathbf{p}^{(3)}$ on the local field enables considerable THG boost in the metasurface as compared to the unpatterned silicon film. This is indeed experimentally observed in the transmitted THG spectrum plotted in Fig. 1c for the metasurface (blue curve) versus the unpatterned film of the same thickness (black curve) cases: an order of magnitude spectrally-integrated THG enhancement is provided by the metasurface. While similar magnitudes of THG enhancement have been observed in the past [46], much more revealing is the *spectrum* of the THG that has never been studied in the context of rapidly-changing metasurfaces.

We observe three features of the THG spectrum that have not been previously experimentally observed or theoretically predicted for a solid-state medium. All three indicate that the THG takes place under non-perturbative conditions, when the optical properties of the metasurface are strongly modified while the laser pulse is interacting with it. *First*, the spectral peak is strongly blue-shifted with respect to its unperturbed $3\omega_L$ (corresponding to $\lambda_{\text{TH}}^{(0)} \approx 1.207 \mu\text{m}$) spectral position measured with an unpatterned film, and with respect to the tripled frequency of the PASIM resonance at $3\omega_R$. *Second*, because the spectral shift of the peak to $\approx 3.05\omega_L$ is larger than the full widths at half maxima (FWHMs) of the unperturbed THG spectrum and of the metasurface resonance, there exists a high-frequency spectral region of the THG (e.g., around $\lambda_{\text{TH}} = 1.18 \mu\text{m}$, on the blue side of the spectral peak) where the THG signal from the metasurface is clearly detectable—more than two orders of magnitude above the noise level—while the THG from the film is below the noise level. *Finally*, the upconver-

sion spectrum reveals another counter-intuitive property of a PASIM: it is possible to resonantly enhance a non-linear process without sacrificing the spectral bandwidth. All three features are related to the emergence of the new, higher energy photons, and can be attributed to photon acceleration due to the dynamic multiphoton FC generation. As a confirmation of the non-perturbative regime, generation of FCs leads to a pronounced power dependence of the transmitted MIR spectra shown in Fig. 1d; we have observed a dissimilar behaviour in bulk silicon (Supplementary Note 4), indicating the key role of the resonance hot spots that enable FC generation through four-photon absorption (4PA).

The concept of PA-induced spectral shifting of the nonlinearly upconverted signal in a metasurface-based semiconductor cavity is schematically illustrated in Fig. 2a. Briefly, MIR photons interact with, and get trapped by, the metasurface. As FCs are generated by 4PA, the resonant frequency of the metasurface blue-shifts, and the frequency of the trapped photons follows. Accelerated MIR photons then upconvert via the standard $\hat{\chi}^{(3)}$ nonlinear process expressed by Eq. (1), resulting in the observed blue-shifting of the THG. To quantify the combined process that manifests as non-integer harmonics generation, we measured the NIR spectra as a function of the incident fluence (Fig. 2c), and compared them with the corresponding spectra generated in the unpatterned Si film (Fig. 2b).

Clearly, the spectral peak and width of the THG light generated in the PASIM can be controlled by incident fluence. The central THG wavelength can be blue-shifted by more than 30 nm, as shown in Fig. 2e, enabling non-integer harmonics generation with center frequencies of up to $\approx 3.1\omega_L$. In contrast with the common belief that the resonant enhancement of the THG must be accompanied by spectral narrowing, our results plotted in Fig. 2f indicate the opposite. The up-converted signal has a spectrum that is up to 50% broader than that from the unstructured film, which is a clear fingerprint of PA. We therefore conclude that the perturbative approach expressed by Eq.(1) fails, suggesting the need for a more accurate model of upconversion.

Theoretical model. The observed blue-shifting, broadening and saturation of the THG spectra can be explained by a simple model involving a single cavity mode with a dipole moment $p(t)$, characterized by its time-dependent resonant frequency $\omega_R(t) \equiv \omega_R^0 + \Delta\omega_R N(t)/N_{\text{max}}$ and damping factor $\gamma_R(t) \equiv \gamma_R^0 + \Delta\gamma_R N(t)/N_{\text{max}}$, and coupled to the incident optical field $\tilde{E}(t)$ according to [47, 48]:

$$\frac{dp(t)}{dt} + [\omega_R(t) + \gamma_R(t)]p(t) = \kappa \tilde{E}(t), \quad (2)$$

where κ is the coupling constant. Here, we assume a Gaussian incident laser pulse with $\tilde{E}(t) = \sqrt{\tilde{I}} \exp(-i\omega_L t - t^2/\tau_L^2)$, where $\tau_L = 105$ fs and $\omega_L =$

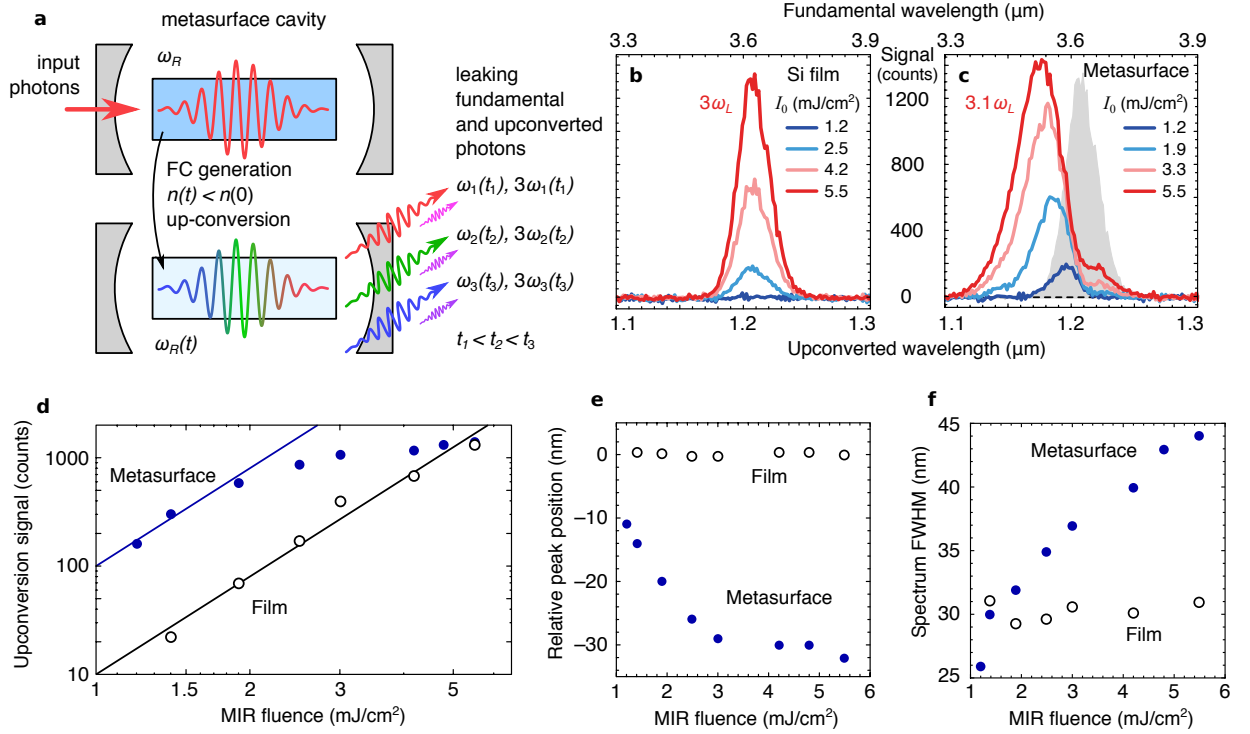


FIG. 2. **Characteristics of non-integer harmonics in PASIMs.** **a**, The multi-step concept of PA-mediated non-integer harmonics generation: MIR photons are trapped by the metasurface cavity, blue-shifted by the rapid refractive index variation due to FC generation inside the metasurface, and then nonlinearly upconverted to NIR photons via the standard THG process. The blue-shifted MIR and NIR photons then leave the metasurface, and their spectra are detected in transmission. The upconversion NIR spectra are measured for four input fluences for the unpatterned Si film **b** and for the metasurface **c**. The spectra are color-coded by the MIR input fluence F . Blue-shifting and spectrum broadening of the THG are observed in metasurfaces but not in the unpatterned film. Shaded grey area in (c): same as in (b) at the highest fluence $F_{\max} = 5.5$ mJ/cm² (corresponding to $I_{\max} = 28$ GW/cm²). **d**, Spectrally integrated THG as a function of the MIR fluence the film (open circles) and metasurface (closed circles), log-log scales. Lines denote the guide-to-the-eye $I_{\text{NIR}} \propto F^3$ dependence. The third-harmonic spectrum experiences blue-shifting shifting (**e**) and broadening (**f**) as a function of F : the metasurface produces ≈ 30 nm spectral shift and $\approx 50\%$ broadening (closed circles), whereas both effects are negligible with unpatterned films (open circles).

ω_R^0 , and \tilde{I} is the appropriately normalized intensity of the pump. The model does not aim to reproduce the peak intensity of the resulting harmonics, which is affected by the absolute normalization of the MIR pulse intensity. The resonant frequency/linewidth shifts are of greater importance for quantitative understanding the PA's role, and their estimation is described below.

The unperturbed ω_R^0 and γ_R^0 are obtained by fitting the transmission spectrum obtained with FTIR (see Fig. 1b), the coupling constant $\kappa = \sqrt{\gamma_R^0}$ [47] neglects non-radiative losses in the absence of FCs, and N_{\max} is the maximum FC density achieved in the experiments. The carrier-induced shifts are assumed to be proportional to carrier density $N(t) < N_{\max}$ produced via the 4PA:

$$N(t) = N_{\max} \frac{2\sqrt{2}}{\tau_L \tilde{I}_{\max}^4 \sqrt{\pi}} \int_{-\infty}^t |\tilde{E}(t')|^8 dt', \quad (3)$$

where \tilde{I}_{\max} is the maximum intensity. We further assume that $\Delta\omega_R = 2 \cdot 10^{13} \text{ s}^{-1}$ and $\Delta\omega_R = 2.5\Delta\gamma_R$; these quan-

tities are close to those obtained by pump-probe measurements (see Supplementary Note 5). The resulting dynamic frequency sweep profiles are shown in Fig. 3a for three characteristic intensities of $\tilde{I} = 8, 14$ and 18 , corresponding to three different regimes of operation of PASIM discussed below.

After numerically solving Eq. (2) to obtain the enhanced near-fields inside the metasurface $\propto p(t)$, we calculate their spectra $|p(\lambda)|^2$ (see Fig. 3b) and observed their significant blue-shifting and spectral broadening with increasing incident intensity \tilde{I} . In the time domain, the latter feature translates into shorter and more intense bursts of the electric field in Si, thus giving rise to more intense nonlinear THG spectra $I_{\text{TH}}(\lambda_{\text{TH}})$ given by

$$I_{\text{TH}}(\lambda_{\text{TH}}) \propto \left| \int_{-\infty}^{\infty} p^3(t) e^{i\omega_{\text{TH}} t} dt \right|^2, \quad (4)$$

where $\lambda_{\text{TH}} = 2\pi c/\omega_{\text{TH}}$. The resulting upconversion spectra are displayed in Fig. 3c,d for three values of the in-

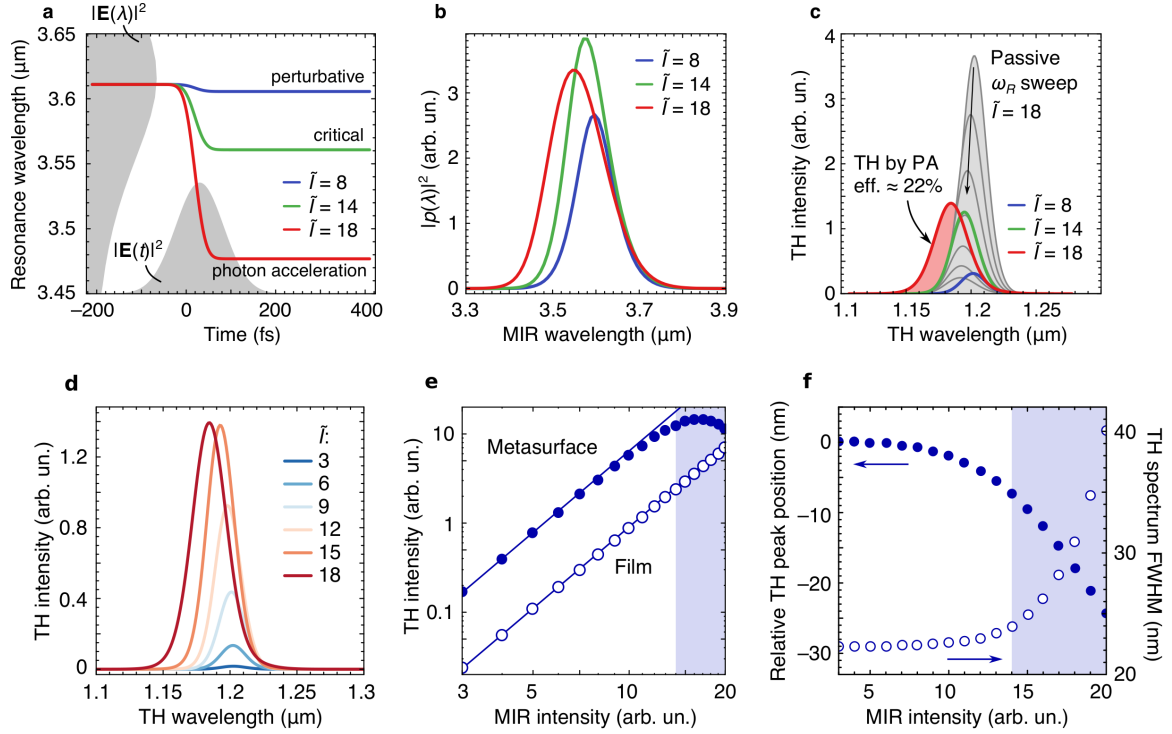


FIG. 3. **Theoretical model of the PA-induced non-integer harmonics generation.** **a**, Time-dependent resonant frequency of the metasurface due to 4PA FC generation plotted for three normalized peak intensities of the MIR pulse: $\tilde{I} = 8$ (perturbative regime, blue curve), $\tilde{I} = 14$ (critical regime, green curve), and $\tilde{I} = 18$ (non-perturbative PA regime, red curve). Shaded areas: the frequency-domain (on the left) and time-domain (on the bottom) profiles of the incident pulse. **b**, Spectra of the MIR electric field inside the metasurface. **c**, **d**, Predicted THG spectra for different input MIR intensities. In **c**, a comparison between the predictions of the models of time-dependent metasurface model (thick lines; coloring as in **a**) and of the time-independent (thin lines) metasurfaces. The family of time-independent metasurfaces satisfies $0 < \Delta\omega_R/\omega_R^0 < 4\%$ and $\tilde{I} = 18$. Filled red area: the portion of the spectrum inaccessible within the time-independent framework. **e**, Peak THG intensity versus input intensity for the unpatterned film (open circles) and resonant metasurface (closed circles). THG from the film is simulated as from a significantly non-resonant structure with $\gamma_R = 10^{15} \text{ s}^{-1}$ with an intensity calibration coefficient that is adjusted for good agreement with the experiment at low intensities. Lines: guide-for-the-eye cubic dependences. **f**, Intensity-dependent THG peak position (closed circles) and THG bandwidth (open circles) generated by the metasurface. Shaded areas in **e** and **f**: the non-perturbative PA regime.

put light intensity \tilde{I} . In Fig. 3c, we reveal the three regimes of PASIM operation by comparing the spectra with those obtained for a set of fixed ω_R . At low intensities, e.g., $\tilde{I} = 8$ (blue curve), the shape of the upconverted spectrum does not differ from that produced by a time-independent metasurface with $\omega_R = \omega_R^0$. As the intensity increases, the upconverted light progressively blue-shifts, and for $\tilde{I} > 14$ (green curve) we start observing PA-induced photons that cannot be produced by any metasurface with time-independent resonances. This point is best illustrated for the intensity $\tilde{I} = 18$ (red curve in Fig. 3c) which is well into the PA regime. We have attempted to reproduce the nonlinear spectrum by using a set of stationary resonant frequencies/linewidths corresponding to different values of N_j/N_{max} , where $1 \leq j \leq 6$. We observe that it is impossible to produce THG photons so far to the blue without invoking photon acceleration.

By comparing the theoretical spectra shown in Fig. 3d

with their experimental counterparts shown in Fig. 2c, we find that the simple model of PA described by Eqs.(1–4) semi-quantitatively captures the key spectral features of the PASIM-based THG: simultaneous increase in intensity, blue-shift, and spectral width with increasing laser intensity. The model rather accurately captures the saturation of the THG as shown in Fig. 3e, the value of the blue-shift ($\sim 25 \text{ nm}$), and the spectral broadening (up to $\sim 40 \text{ nm}$) as shown in Fig. 3f. Even though the dynamic resonance sweep is a very complex process, especially because of the highly localized nature of FC generation, we have demonstrated that our model can explain the main features of the experiment, and can be potentially used for optimizing future metasurface designs.

DISCUSSION

We have estimated the energy portion of the up-converted radiation that is unreachable by a passive frequency sweep ($\approx 22\%$) by calculating the shaded area in Fig. 3c relative to the area under the gray curves. Improving the efficiency of PA-based upconversion is clearly beneficial because, while passive resonant structures can improve the conversion efficiency at the expense of the bandwidth, the PASIM-based approach does not suffer from such fundamental limitation. Several tools are available for improving the photons' capture and acceleration. One approach is to reduce $\Delta\gamma_R$ by using materials with longer carrier scattering time (e.g., GaAs). A more intriguing approach is utilize optical pulse shaping [49], thereby engineering both the right-hand side (via frequency chirping) and the left-hand side (via the amplitude envelope shaping and temporal engineering of FC density) of Eq. (2). We conjecture that the latter approach is sufficiently flexible to provide superb control over the efficiency and spectrum of the PA-induced nonlinear light generation, thus paving the way for novel and compact frequency conversion devices. By expanding the toolbox of nonlinear optical processes in nanostructures to include photon acceleration, as experimentally demonstrated and analytically modeled here for the first time, we envision a wide range of applications in photonics, in mid-infrared and beyond.

ACKNOWLEDGEMENTS

This work was supported by the Office of Naval Research (ONR) and by the Air Force Research Laboratory (AFRL). This work was performed in part at the Cornell NanoScale Facility, a member of the National Nanotechnology Coordinated Infrastructure (NNCI), which is supported by the National Science Foundation (Grant ECCS-1542081).

AUTHOR CONTRIBUTIONS

M.R.S. and G.S. conceived the idea. M.R.S. fabricated the sample and characterized it using FTIR spectroscopy. M.R.S., K.W., N.T. and E.C. performed the nonlinear optical measurements. Z.F. performed COMSOL simulations. M.R.S. performed CMT calculations. All authors contributed to the preparation of the manuscript.

METHODS

Sample fabrication and characterization Samples of silicon metasurfaces were fabricated at the Cornell Nanoscale Facility (CNF) from a silicon-on-insulator wafer (600 nm undoped Si device layer on top of a $460\text{ }\mu\text{m}$ top-grade sapphire from University Wafer) using the following recipe. The substrate was cleaned with acetone, isopropanol and O_2 plasma; PMMA 495 was spun to form a 400-nm-thick layer and baked for 15 min at 170°C ; PMMA 950k was spun to form a 100-nm-thick layer and baked for 15 min at

170°C ; E-spacer conducting layer was spun at 6000 rpm; the pattern was exposed at $1000\text{ }\mu\text{C}/\text{cm}^2$ (JEOL 9500FS) and development was performed with MIBK:IPA 1:3 solution; a 60-nm-thick Cr mask was electron-beam-evaporated and lifted off in sonicated acetone for 1 minute; the pattern was transferred to the silicon layer through HBr reactive ion etch (Oxford Cobra). Finally, Cr was removed with the commercially available Cr wet etchant.

Infrared spectroscopy Bruker Vertex 80 FTIR spectrometer was upgraded to an external transmittance spectroscopy setup as described elsewhere [38] that enables collimated MIR spectroscopy, with the MIR beam focused to a spot size of about $300\text{ }\mu\text{m}$ in diameter using a pinhole imaging technique. The transmitted beam was sent to the detector and Fourier-analyzed by the spectrometer. Normalization was done using the signal from the clear sapphire area.

Nonlinear optical measurements Setup schematic and a comprehensive description of the nonlinear optical measurements are given in Supplementary Figure 3 and Supplementary Note 3, respectively.

Finite element simulations We used COMSOL Multiphysics to model the response of the metasurfaces (no free carriers) by defining the computational domain as a slab with the dimensions of $p_x \times p_y \times 3\text{ }\mu\text{m}$, where $p_x = 2.1\text{ }\mu\text{m}$ and $p_y = 2\text{ }\mu\text{m}$. Periodic boundary conditions were used for the domain boundaries parallel to the $x-z$ and $y-z$ planes, and perfectly matched layers (PMLs) were used for the domain boundaries parallel to the $x-y$. The dimensions of the metasurface were chosen to match those obtained from the SEM image. Wavelength-independent refractive indices of $n_{\text{Si}} = 3.45$ and $n_{\text{Sapp}} = 1.7$ were used for Si and sapphire, respectively.

* mrs356@cornell.edu

† gs656@cornell.edu

- [1] Franken, P. A., Hill, A. E., Peters, C. W. & Weinreich, G. Generation of optical harmonics. *Phys. Rev. Lett.* **7**, 118–119 (1961).
- [2] Maker, P. & Terhune, R. Study of Optical Effects Due to an Induced Polarization Third Order in the Electric Field Strength. *Phys. Rev.* **137**, 344–350 (1965).
- [3] Burnett, N. H., Baldis, H. A., Richardson, M. C. & Enright, G. D. Harmonic generation in CO₂ laser target interaction. *Appl. Phys. Lett.* **31**, 172–174 (1977).
- [4] Yamada, M., Nada, N., Saitoh, M. & Watanabe, K. First-order quasi-phase matched LiNbO₃ waveguide periodically poled by applying an external field for efficient blue second-harmonic generation. *Appl. Phys. Lett.* **62**, 435–436 (1993).
- [5] Campagnola, P. J. & Loew, L. M. Second-harmonic imaging microscopy for visualizing biomolecular arrays in cells, tissues and organisms. *Nature Biotechnol.* **21**, 1356–1360 (2003).
- [6] Débarre, D. *et al.* Imaging lipid bodies in cells and tissues using third-harmonic generation microscopy. *Nature Methods* **3**, 47–53 (2006).
- [7] Heinz, T. F., Chen, C. K., Ricard, D. & Shen, Y. Spectroscopy of Molecular Monolayers by Resonant Second-Harmonic Generation. *Phys. Rev. Lett.* **48**, 478–481 (1982).
- [8] Shen, Y. R. Surface properties probed by second-harmonic and sum-frequency generation. *Nature* **337**, 519–525 (1989).
- [9] Stiopkin, I. *et al.* Hydrogen bonding at the water surface revealed by isotopic dilution spectroscopy. *Nature* **474**,

- 192—195 (2011).
- [10] Mendonça, J. T. *Theory of Photon Acceleration* (Institute of Physics Publishing, Bristol and Philadelphia, 2000).
 - [11] Yablonovitch, E. Self-Phase Modulation of Light in a Laser-Breakdown Plasma. *Phys. Rev. Lett.* **32**, 1101–1104 (1974).
 - [12] Wilks, S. C., Dawson, J. M., Mori, W. B., Katsouleas, T. & Jones, M. E. Photon accelerator. *Phys. Rev. Lett.* **62**, 2600–2603 (1989).
 - [13] Felsen, L. B. & Whitman, G. M. Wave Propagation in Time-Varying Media. *IEEE Trans. Antennas Propag.* **AP-18**, 242–253 (1970).
 - [14] Wood, W., Siders, C. & Downer, M. Measurement of Femtosecond Ionization Dynamics of Atmospheric Density Gases by Spectral Blueshifting. *Phys. Rev. Lett.* **67**, 3523–3536 (1991).
 - [15] Savage, R. L., Joshi, C. & Mori, W. B. Frequency up-conversion of electromagnetic radiation upon transmission into an ionization front. *Phys. Rev. Lett.* **68**, 946–949 (1992).
 - [16] Yablonovitch, E. Spectral broadening in the light transmitted through a rapidly growing plasma. *Phys. Rev. Lett.* **31**, 877–879 (1973).
 - [17] Siders, C. W. *et al.* Blue-shifted third-harmonic generation and correlated self-guiding during ultrafast barrier suppression ionization of subatmospheric density noble gases. *J. Opt. Soc. Am. B* **13**, 330–335 (1996).
 - [18] Preble, S. F., Xu, Q. & Lipson, M. Changing the colour of light in a silicon resonator. *Nature Photon.* **1**, 293–296 (2007).
 - [19] Tanabe, T., Notomi, M., Taniyama, H. & Kuramochi, E. Dynamic release of trapped light from an ultrahigh-Q nanocavity via adiabatic frequency tuning. *Phys. Rev. Lett.* **102**, 043907 (2009).
 - [20] Dong, P., Preble, S. F., Robinson, J. T., Manipatruni, S. & Lipson, M. Inducing Photonic Transitions between Discrete Modes in a Silicon Optical Microcavity. *Phys. Rev. Lett.* **100**, 033904 (2008).
 - [21] Holloway, C. L. *et al.* An overview of the theory and applications of metasurfaces: The two-dimensional equivalents of metamaterials. *IEEE Antennas Propag. Mag.* **54**, 10–35 (2012).
 - [22] Kildishev, A. V., Boltasseva, A. & Shalaev, V. M. Planar Photonics with Metasurfaces. *Science* **339**, 1232009 (2013).
 - [23] Yu, N. & Capasso, F. Flat optics with designer metasurfaces. *Nat. Mater.* **13**, 139–50 (2014).
 - [24] Li, G., Zhang, S. & Zentgraf, T. Nonlinear photonic metasurfaces. *Nat. Rev. Mater.* **2**, 17010 (2017).
 - [25] Krasnok, A., Tymchenko, M. & Alu, A. Nonlinear Metasurfaces: A Paradigm Shift in Nonlinear Optics. *Mater. Today* in print (2017).
 - [26] Yu, N. *et al.* Light Propagation with Phase Discontinuities: Generalized Laws of Reflection and Refraction. *Science* **334**, 333–337 (2011).
 - [27] Emani, N. K. *et al.* Electrically tunable damping of plasmonic resonances with graphene. *Nano Letters* **12**, 5202–5206 (2012).
 - [28] Yao, Y. *et al.* Broad electrical tuning of graphene-loaded plasmonic antennas. *Nano Letters* **13**, 1257–1264 (2013).
 - [29] Dabidian, N. *et al.* Electrical switching of infrared light using graphene integration with plasmonic Fano resonant metasurfaces. *ACS Photon.* **2**, 216–227 (2015).
 - [30] Dabidian, N. *et al.* Experimental demonstration of phase modulation and motion sensing using graphene-integrated metasurfaces. *Nano Lett.* **16**, 3607–3615 (2016).
 - [31] Klein, M. W., Enkrich, C., Wegener, M. & Linden, S. Second-harmonic generation from magnetic metamaterials. *Science* **313**, 502–504 (2006).
 - [32] Lee, J. *et al.* Giant nonlinear response from plasmonic metasurfaces coupled to intersubband transitions. *Nature* **511**, 65–69 (2014).
 - [33] Vampa, G. *et al.* Plasmon-enhanced high-harmonic generation from silicon. *Nat. Phys.* **13**, 659–662 (2017).
 - [34] Wurtz, G. A. *et al.* Designed ultrafast optical nonlinearity in a plasmonic nanorod metamaterial enhanced by nonlocality. *Nat. Nanotechnol.* **6**, 106–110 (2011).
 - [35] Guo, P., Schaller, R. D., Ketterson, J. B. & Chang, R. P. H. Ultrafast switching of tunable infrared plasmons in indium tin oxide nanorod arrays with large absolute amplitude. *Nat. Photon.* **10**, 267–273 (2016).
 - [36] Shcherbakov, M. R. *et al.* Ultrafast all-optical tuning of direct-gap semiconductor metasurfaces. *Nat. Commun.* **8**, 17 (2017).
 - [37] Kuznetsov, A. I., Miroshnichenko, A. E., Brongersma, M. L., Kivshar, Y. S. & Lukyanchuk, B. Optically resonant dielectric nanostructures. *Science* **354**, aag2472 (2016).
 - [38] Wu, C. *et al.* Spectrally selective chiral silicon metasurfaces based on infrared Fano resonances. *Nat. Commun.* **5**, 3892 (2014).
 - [39] Yang, Y., Kravchenko, I. I., Briggs, D. P. & Valentine, J. All-dielectric metasurface analogue of electromagnetically induced transparency. *Nat. Commun.* **5**, 5753 (2014).
 - [40] Shcherbakov, M. R. *et al.* Enhanced Third-Harmonic Generation in Silicon Nanoparticles Driven by Magnetic Response. *Nano Lett.* **14**, 6488–6492 (2014).
 - [41] Liu, S. *et al.* Resonantly Enhanced Second-Harmonic Generation Using III–V Semiconductor All-Dielectric Metasurfaces. *Nano Lett.* **16**, 5426–5432 (2016).
 - [42] Grinblat, G., Li, Y., Nielsen, M. P., Oulton, R. F. & Maier, S. A. Efficient Third Harmonic Generation and Nonlinear Sub-Wavelength Imaging at a Higher-Order Anapole Mode in a Single Germanium Nanodisk. *ACS Nano* **11**, 953–960 (2016).
 - [43] Makarov, S. V. *et al.* Efficient Second-Harmonic Generation in Nanocrystalline Silicon Nanoparticles. *Nano Lett.* **17**, 3047–3053 (2017).
 - [44] Shalaev, M. I. *et al.* High-Efficiency All-Dielectric Metasurfaces for Ultracompact Beam Manipulation in Transmission Mode. *Nano Lett.* **15**, 6261–6266 (2015).
 - [45] Neuner, B. *et al.* Efficient infrared thermal emitters based on low-albedo polaritonic meta-surfaces. *Appl. Phys. Lett.* **102**, 211111 (2013).
 - [46] Shorokhov, A. S. *et al.* Multifold Enhancement of Third-Harmonic Generation in Dielectric Nanoparticles Driven by Magnetic Fano Resonances. *Nano Letters* **16**, 4857–4861 (2016).
 - [47] Haus, H. A. *Waves And Fields In Optoelectronics* (Prentice-Hall, New Jersey, 1984).
 - [48] Minkov, M., Shi, Y. & Fan, S. Exact solution to the steady-state dynamics of a periodically-modulated resonator. *APL Photonics* **2**, 076101 (2017).
 - [49] Weiner, A. M. Femtosecond pulse shaping using spatial light modulators. *Rev. Sci. Instrum.* **71**, 1929 (2000).

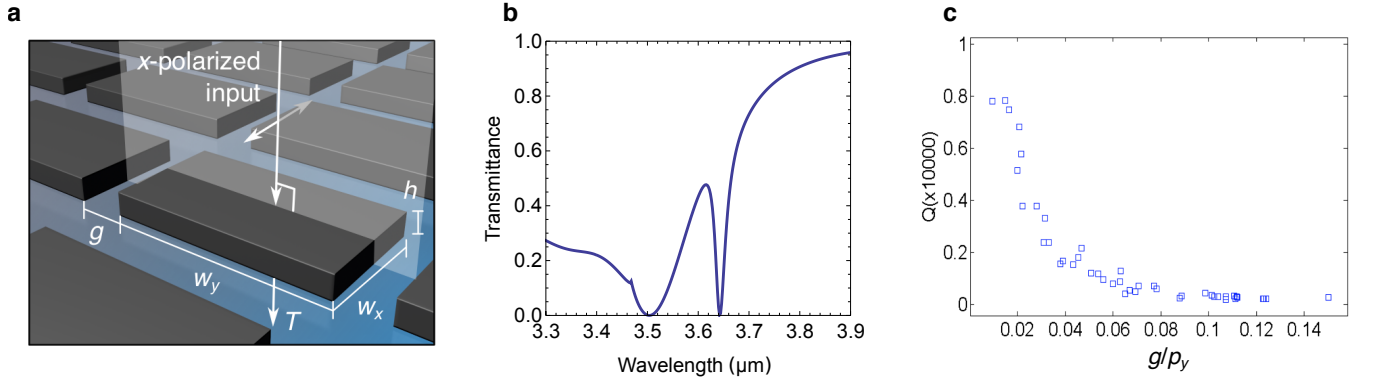
Supplementary Note 1

High-Q Metasurface Design

The main considerations for the design of the photon accelerating semiconductor infrared metasurfaces (PASIMs) were outlined in similar realisations of high-Q semiconductor nanoparticle arrays [1, 2]. The basic physics behind crafting a high-quality-factor metasurface is to create a planar waveguide system with a route to couple light in and out by periodic corrugations. A very simple system we will consider here consists of conventional rectangular silicon waveguides with periodic through-notches that match the momentum of the initially normally incident light to a waveguide mode:

$$\frac{2\pi}{p_y} = \beta(\omega), \quad (5)$$

where p_y is the periodicity of corrugations and $\beta(\omega)$ is the propagation constant of the waveguide mode; see the structure of the metasurface in Supplementary Figure 4a. As a result, for the frequencies that satisfy Eq. (5), strong transmission dips are observed, as shown for a metasurface with $w_x = 0.84 \mu\text{m}$, $w_y = 1.82 \mu\text{m}$, $p_x = 2 \mu\text{m}$, $p_y = 2.1 \mu\text{m}$, $h = 0.6 \mu\text{m}$ in Supplementary Figure 4b. By changing the gap width g , one can tune the coupling between the cuboids, hence, affecting the Q -factor of the resonance, as shown in Supplementary Figure 4c.

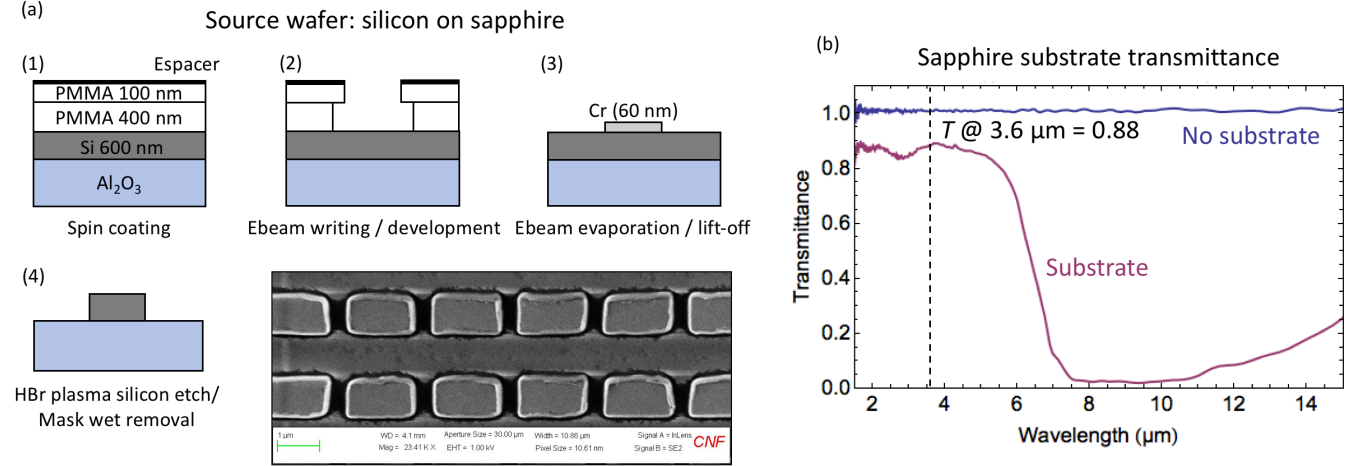


Supplementary Figure 4. **a**, The geometry of the PASIM with the dimensions and illumination parameters outlined. **b**, The calculated transmittance spectra of the PASIM used in the experiments. A sharp transmittance dip is seen at the coupling wavelength around $\lambda = 3.64 \mu\text{m}$. **c**, Q -factor of the resonance dip as a function of the relative gap width g/p_y . At $p_y = 2.1 \mu\text{m}$, for 20-nm-wide gaps, the Q -factor can be as high as $8 \cdot 10^3$.

Supplementary Note 2

Sample Fabrication

The PASIM fabrication procedure is described in the Methods section of the main text of the paper. In Supplementary Figure 5(a), the schematic of the fabrication process is illustrated. In Supplementary Figure 5(b), the choice of the sapphire substrate is justified by showing highly transparent operation for the mid-infrared radiation with $\lambda \approx 3.6 \mu\text{m}$.



Supplementary Figure 5. (a) Sample fabrication process. (b) Transmittance of the sapphire substrate (purple curve) showing large transmittance in the spectral region around $3.6 \mu\text{m}$.

Supplementary Note 3

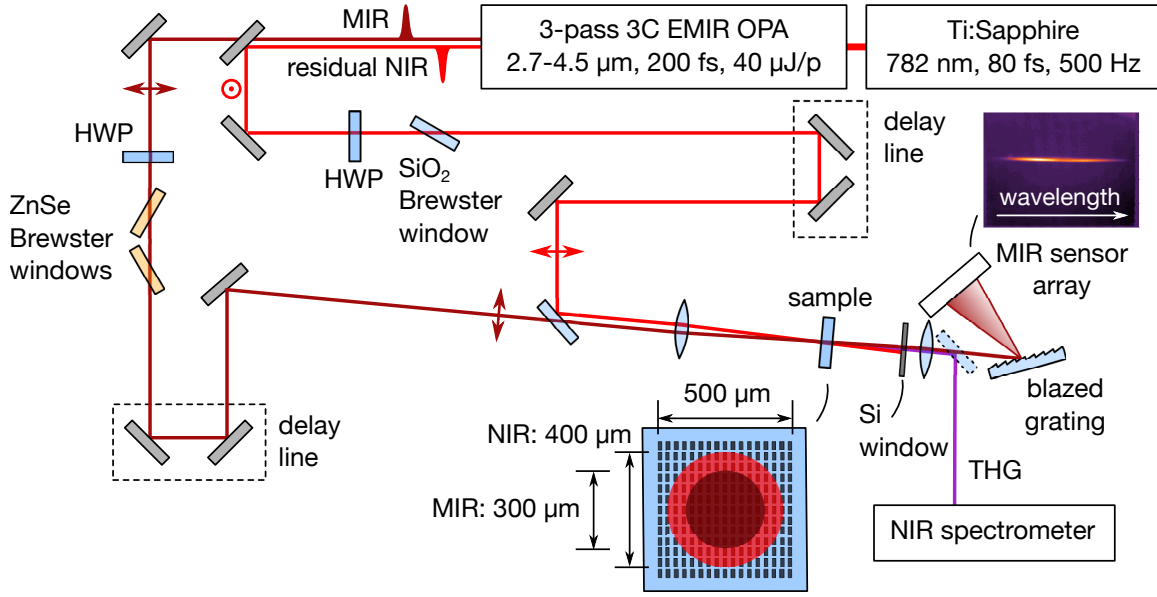
Nonlinear-Optical Measurements

In Supplementary Figure 6, a schematic of the optical setup used for nonlinear measurements is shown. The Extreme Mid-IR (EMIR) optical parametric amplifier (OPA) is a homebuilt KNbO_3/KTA 3-crystal/3-pass OPA. EMIR is pumped by The Ohio State University's GRAY laser, a homebuilt 80-fs Ti:Sapphire chirped pulse amplification system with a central wavelength of 780 nm and 4 mJ/pulse. The repetition rate of EMIR can be varied nearly continuously between 1 and 500 Hz using an external Pockels-cell-based pulse picker. EMIR was used to generate 200-fs mid-IR pulses with up to 40 μJ /pulse. The output wavelength of EMIR can be varied continuously from $\lambda = 2.7$ to 4.5 μm . For the experiments, the MIR (idler) beam was fixed at $\lambda = 3.62$ μm . The 780 nm NIR, MIR, and $\lambda = 1$ μm (signal) output beams are separated spatially, with the 1- μm signal being dumped and 780 nm pump being retained for use in pump-probe experiments. The residual NIR and MIR beams are roughly collimated to a size of about 2.5 mm. The NIR pulses were found to have a pulse duration of 200 ± 15 fs.

Output modes were characterized for several different wavelengths using a WinCamD-FIR2-16-HR 2 to 16 μm Beam Profiler System. Residual NIR pulse length was characterized using a BBO crystal based near-IR autocorrelator. MIR pulse duration was measured using an AGS crystal based MIR autocorrelator for 3 and 3.6 μm .

MIR spectra were obtained using a home-built spectrometer based on a ThorLabs GR1325-30035 blazed ruled diffraction grating with a blaze wavelength of 3.5 μm as the dispersion element and the beam profiler sensor as the detector array. On the setup schematic, an inset demonstrates a typical image of the diffracted MIR beam. The spectrometer was calibrated with an A.P.E. Wavescan USB MIR spectrometer, which, due to a low sensitivity and operation speed, could not be used for the routine MIR spectroscopy.

For pump-probe and upconversion spectroscopy, the horizontally polarized MIR pulses first pass through a waveplate-polarizer assembly for precise energy control. The pulses travel through a variable delay line after which they are recombined with the NIR pulses via a dichroic mirror. The NIR pulses follow a separate but similar path. The collinear beams are focused using a CaF_2 $f = 100$ mm plano-convex lens. In the sample plane, the spot sizes were found to be 300 μm FWHM for MIR and 400 μm FWHM for NIR. Both spots fit within the 500×500 μm structured area of the metasurfaces. The relative delay between MIR and NIR pulses was controlled dynamically using either the manual MIR delay line or the electronically controlled NIR delay line with sub-ps resolution. For self-tuning of the resonance, the NIR beam is blocked with a beam block. MIR fluences were varied from 1 to 7 mJ/cm² and NIR fluences were varied from < 1 to 4 mJ/cm² for



Supplementary Figure 6. Optical setup based on a Ti:Sapphire amplifier system coupled to an optical parametric amplifier (OPA) capable of producing femtosecond laser pulses with the carrier wavelength tunable from 2.7 to 4.5 μm . Half-wave plates (HWP) are used for power management of both pump and probe beams.

the experiments. As a control method, a Si wafer was pumped in place of the sample. With NIR beam blocked, contamination of scattered light from the NIR and 1 μm signal was measured at the sample location. The NIR content was found to be 0.5 pJ per pulse and 1 μm signal was estimated to be of order 1 pJ/pulse. These pulse energies were determined to be insignificant to affect the sample during the experiment.

Upon transmission through the sample, the MIR beam and any upconversion signal were collected with a CaF_2 $f = 50$ mm bi-convex lens. Any residual NIR was filtered using a Si window. In one configuration, a blazed grating/MIR camera combination is used as a high resolution MIR spectrometer. In another configuration, a commercial Ocean Optics NirQuest spectrometer (900–2500 nm) is used for detection of the upconverted radiation.

Supplementary Note 4

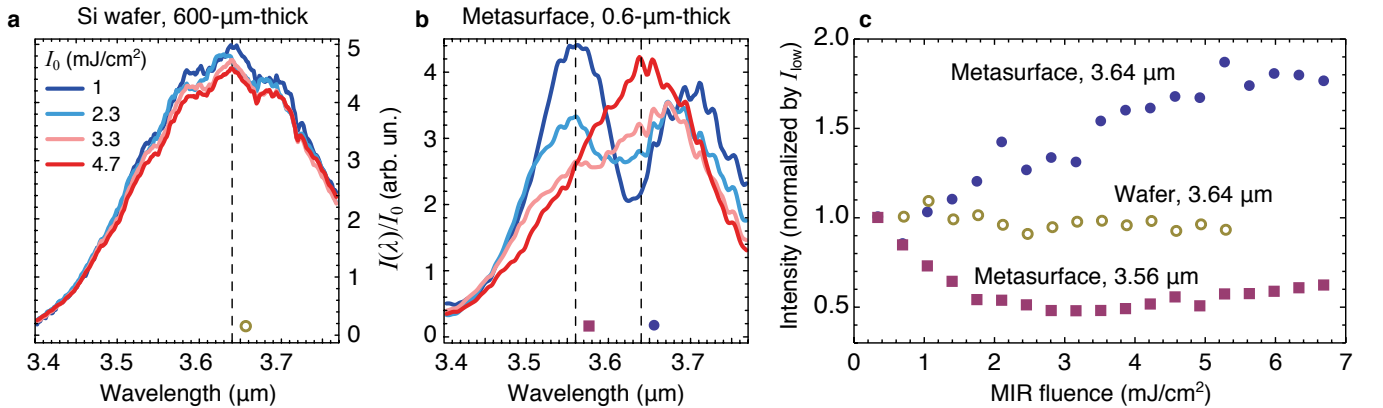
Power-Dependent Transmittance of the PASIM Enabled by Four-Photon Absorption

The nonlinear properties of the PASIM can be interpreted only after the physics behind the resonance modification by mid-IR pulses is fully understood. This is facilitated by measuring the transmitted pulse spectra as a function of the incident pulse fluence (see Supplementary Figure 7) which controls the FC generation. Note that undoped silicon has negligible linear absorbance [3] in the studied spectral range because the bandgap of silicon $E_g = 1.12$ eV is more than three times larger than the MIR pulse carrier energy of $\hbar\omega = 0.35$ eV. Therefore, the interaction of MIR pulses with the metasurfaces is only affected by high-order processes, such as the four-photon absorption (4PA). We make estimates of the FC concentration via:

$$N = 2F(1 - e^{-\alpha h})/4hE_{\text{pump}}, \quad (6)$$

where F is the incident pulse fluence, α is the 4PA-induced absorption constant, h is the thickness of the medium, and E_{pump} is the energy of a pump photon; the factor of 2 stands for a pair of generated FCs and the factor of 4 stands for the four photons needed for an absorption act. The 4PA-induced absorption is calculated with $\alpha = \beta_4 I^3$, where $\beta_4 = 3.5 \cdot 10^{-4} \text{ cm}^5/\text{GW}^3$ is the 4PA coefficient [4] and I is the input intensity. At an intensity of $I = 10 \text{ GW}/\text{cm}^2$ (fluence $F \approx 2 \text{ mJ}/\text{cm}^2$), in a bulk silicon wafer, $\alpha = 3.5 \text{ cm}^{-1}$, and the FC density is only $N \approx 3 \cdot 10^{16} \text{ cm}^{-3}$. Not surprisingly, essentially no self-modulation was observed for the $600 \text{ }\mu\text{m}$ -thick silicon wafer, as shown in Supplementary Figure 7a for four fluence values.

However, the hot spots inside the metasurface (Fig.1a,b of the main text) enable a much higher



Supplementary Figure 7. **a**, Spectra of MIR pulses transmitted through a $500\text{-}\mu\text{m}$ -thick silicon wafer, divided by the input pulse fluence. **b**, Spectra of MIR pulses transmitted through a 600-nm -thick silicon metasurface MS1, divided by the input pulse fluence. The same set of pump fluences is used as in panel **a**. A dip that starts off $\lambda = 3.64 \text{ }\mu\text{m}$ corresponds to the high-Q resonance observed in the FTIR transmittance spectrum in Fig. 1b of the main text. **c**, A comparison of the fluence-dependent transmittance on the resonance ($\lambda = 3.64 \text{ }\mu\text{m}$, closed circles) and off the resonance ($\lambda = 3.56 \text{ }\mu\text{m}$, closed squares) to that of the wafer at $\lambda = 3.64 \text{ }\mu\text{m}$ (open circles).

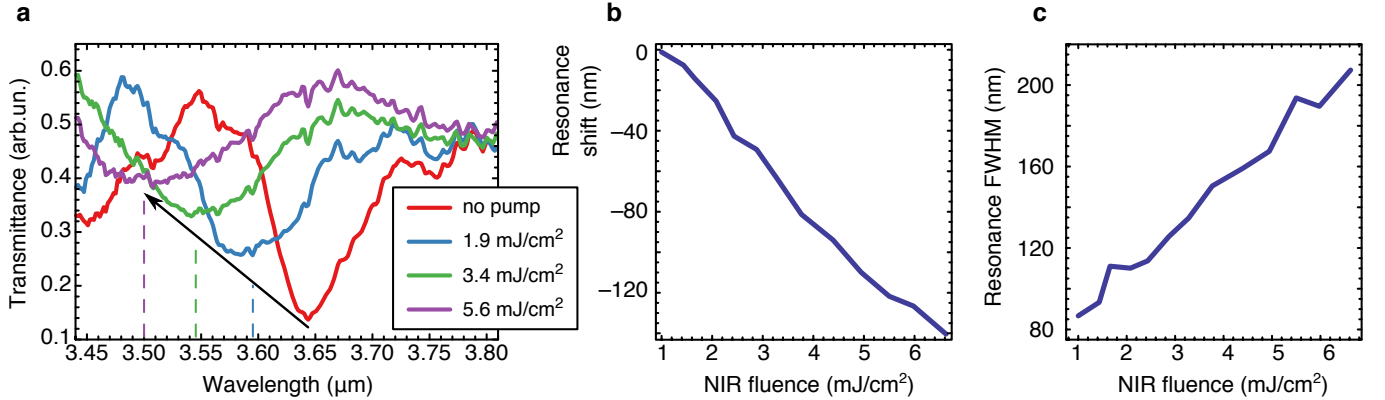
FC density. With the local intensity of $I_{\text{local}} = 3.5 \text{ TW/cm}^2$ (mind the 350 enhancement factor in Fig. 1b of the main text), the 4PA-induced absorption constant peaks at $\alpha \approx 10^{10} \text{ cm}^{-1}$, which would induce full absorption of the incident pulse with the hot spots. Of course, Supplementary Eq.(2) fails under high intensities due to saturation of β_4 ; however, the hint is that giant self-modulations of MIR pulses are possible in our metasurfaces. Such fluence-dependent modifications of the resonance frequency and lifetime are shown in Supplementary Figure 7b. At low fluences (blue curve), the transmitted pulse contains a dip at $\lambda_{\text{dip}} = 3.64 \text{ }\mu\text{m} \approx \lambda_R$, which is in good agreement with the FTIR measurements. At higher fluences, the dip experiences considerable modifications, including blue-shift and broadening, and at the maximum fluence of $F = 5.5 \text{ mJ/cm}^2$, the dip is seen no more, as it has moved out of the spectral bandwidth of the mir-IR pulses.

Additionally, even at the lowest fluence, there is clear evidence of the PA. Specifically, the spectral component of the transmitted pulse are clearly redistributed from the dip region to a new *global peak* at $\lambda_{\text{peak}} = 3.56 \text{ }\mu\text{m}$ which is absent in the linear transmittance spectrum shown in Fig. 1b of the main text. This suggests that a significant fraction of the photons from the most populated portion of the original spectrum around $\lambda = \lambda_L$ are trapped by the metasurface resonance, and then accelerated to shorter wavelengths by the resonance blue-shifting during the FC generation. For this process to be efficient, femtosecond control of the FC generation is crucial. Specifically, it is important that significant FC generation takes place around the peak of the laser intensity. If it starts too early in the pulse, then by the arrival time t_{max} of the intensity maximum of the MIR pulse, the metasurface resonance frequency $\omega_R(t = t_{\text{max}})$ will have shifted too far to the blue (where the number of the incident photons is small), and will have decreased its quality factor $Q_R(t = t_{\text{max}})$ to the value that is insufficient for photon trapping.

Supplementary Note 5

Plasma-Induced Blue-Shift and Damping of the Resonance

We can appreciate the values for the FC-induced metasurface resonance modification by measuring the MIR pulse transmittance spectra upon FC injection by an external NIR pump. The spectra of the pulses transmitted through the sample were measured at different pump powers and/or pump–probe delays. The acquired spectra were divided by the initial spectrum of the pulses transmitted through the substrate. In order to extract the position of the resonance, we fitted the spectra near the dips by a parabolic dependence, which is the second-order Taylor expansion of the Lorentzian line shape. An example of the curves after the division, along with the fit-extracted dip positions, is shown in Supplementary Figure 8. The maximum wavelength shift was observed to be $\Delta\lambda = 140$ nm, or $\Delta\omega_R = 2\pi c\lambda^{-2}\Delta\lambda \approx 1.8 \cdot 10^{13} \text{ s}^{-1}$. The resonance damping factor was calculated from the manually defined FWHM of the resonance. Having taken into account the unperturbed value of $\gamma_R^0 = 7 \cdot 10^{12} \text{ s}^{-1}$, the maximum addend to the resonance damping is estimated at $\Delta\gamma_R \approx 7.5 \cdot 10^{12} \text{ s}^{-1}$. In the modeling, to reasonably reproduce the experimental results, we found it necessary to use the following values: $\Delta\omega_R = 2 \cdot 10^{13} \text{ s}^{-1}$ and $\Delta\gamma_R^0 = 5 \cdot 10^{12} \text{ s}^{-1}$, which are fairly close to those obtained by the pump–probe measurements.

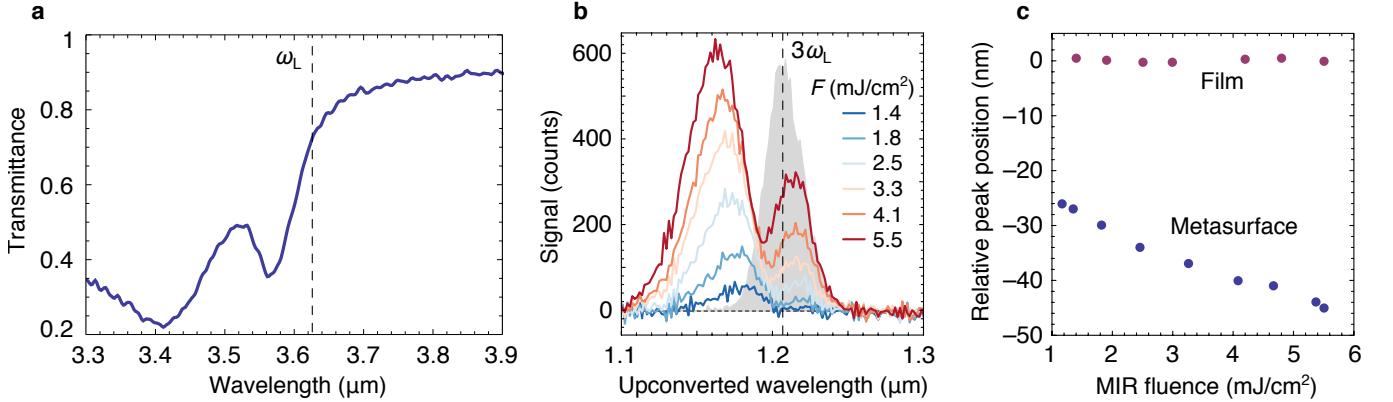


Supplementary Figure 8. **a**, Pump-induced transmittance changes in the metasurfaces. **b**, Retrieved resonance shift as a function of the near-IR beam fluence. **c**, Retrieved resonance FWHM as a function of the near-IR beam fluence.

Supplementary Note 6

Blue-shifted harmonics from a weakly resonant PASIM

We perform measurements of power-dependent upconversion spectra for a metasurface with a different set of parameters, which allows for a resonance at $\lambda_R = 3.56 \mu\text{m}$ that is slightly misplaced with respect to the central pump wavelength of $\lambda_L = 3.62 \mu\text{m}$, see Supplementary Figure 6a. We observe a behaviour of the power-dependent upconversion similar to that of the resonant metasurface: the maximum of the spectrum gets blue-shifted as the pump fluence increases. The following differences can be seen, though. First, there are two peaks in each spectrum. We associate the second peak that is close to the original, non-PA THG, to be a non-resonant contribution to the THG from the detuned sample. Similarly to the unstructured film case, its position stays within a corridor of 2 nm throughout the measurements. Second, the absolute THG intensity is by approximately a factor of two less than that from the resonant sample. And third, the dependence of the central position of the main THG peak does not seem to saturate as a function of fluence. This indicates that there is no charge saturation under these conditions, which might be the case for a resonant PASIM.



Supplementary Figure 9. **a**, FTIR transmittance spectrum of a weakly resonant PASIM sample. The dip at $\lambda_R = 3.56 \mu\text{m}$ indicates the collective mode of the metasurface. **b**, Upconversion as a function of MIR fluence for a weakly resonant PASIM sample. **c**, The position of the main upconversion peak in panel **b** as a function of pump fluence (blue dots). The same dependence measured for an unstructured film is given with purple dots.

SUPPLEMENTARY REFERENCES

* mrs356@cornell.edu

† gs656@cornell.edu

- [1] Y. Yang, I. I. Kravchenko, D. P. Briggs, and J. Valentine, Nat. Commun. **5**, 5753 (2014).
- [2] M. Parry, A. Komar, B. Hopkins, S. Campione, S. Liu, A. E. Miroshnichenko, J. Nogan, M. B. Sinclair, I. Brener, and D. N. Neshev, Appl. Phys. Lett. **111**, 053102 (2017).
- [3] R. A. Soref, S. J. Emelett, and A. R. Buchwald, J. Opt. A **8**, 840 (2006).
- [4] X. Gai, Y. Yu, B. Kuyken, P. Ma, S. J. Madden, J. Van Campenhout, P. Verheyen, G. Roelkens, R. Baets, and B. Luther-Davies, Laser Photon. Rev. **7**, 1054 (2013).